

Magnetic structure and exchange interactions in the Heisenberg pyrochlore antiferromagnet $\text{Gd}_2\text{Pt}_2\text{O}_7$

Philip G. Welch,^{1,2} Joseph A. M. Paddison,³ Manh Duc Le,² Jason S. Gardner,³ Wei-Tin Chen⁴,⁴ Andrew R. Wildes,⁵ Andrew L. Goodwin¹,¹ and J. Ross Stewart^{1,2,*}

¹*Inorganic Chemistry Laboratory, University of Oxford, South Parks Road, Oxford OX1 3QR, United Kingdom*

²*ISIS Neutron and Muon Facility, Science and Technology Facilities Council, Rutherford Appleton Laboratory, Didcot OX11 0QX, United Kingdom*

³*Materials Science and Technology Division, Oak Ridge National Laboratory, Oak Ridge, Tennessee 37831, USA*

⁴*Centre for Condensed Matter Sciences, National Taiwan University, Taipei 10617, Taiwan, Republic of China*

⁵*Institut Laue-Langevin, CS 20156, F-38042 Grenoble Cedex 9, France*



(Received 21 December 2021; revised 14 February 2022; accepted 16 February 2022; published 1 March 2022)

The Heisenberg pyrochlore antiferromagnet $\text{Gd}_2\text{Pt}_2\text{O}_7$ is one of a series of gadolinium pyrochlore compounds with a variety of B-site cations. Despite the expected simplicity of a spin-only Gd^{3+} Heisenberg interaction model, the gadolinium pyrochlore series exhibits various complex magnetic ground states at low temperature. $\text{Gd}_2\text{Pt}_2\text{O}_7$ displays the highest temperature magnetic order of the series with $T_N = 1.6$ K, which has been attributed to enhanced superexchange pathways facilitated by empty $5d e_g$ Pt orbitals. In this study, we use various neutron scattering techniques on an isotopically enriched polycrystalline $^{160}\text{Gd}_2\text{Pt}_2\text{O}_7$ sample to examine the magnetic structure and spin-wave excitation spectrum below T_N in order to extract the dominant exchange interactions. We find that the ground-state magnetic structure is the Palmer-Chalker state previously seen in $\text{Gd}_2\text{Sn}_2\text{O}_7$ with an associated gapped excitation spectrum consistent with enhanced exchange interactions between further near-neighbor Gd^{3+} ions. We confirm this exchange model with analysis of the magnetic diffuse scattering in the paramagnetic regime using polarized neutrons.

DOI: [10.1103/PhysRevB.105.094402](https://doi.org/10.1103/PhysRevB.105.094402)

I. INTRODUCTION

The magnetic pyrochlore lattice—in which magnetic ions sit on a lattice of corner-sharing tetrahedra (see Fig. 1)—is commonly studied as an archetypal example of three-dimensional geometrical magnetic frustration. The study of these so-called “highly frustrated magnets” provides a route to access a large variety of fascinating emergent low-temperature magnetic states including spin-liquids, spin-glasses, spin-ices, and fragmented spin-structures [1–5].

The Gd-pyrochlore series of compounds $\text{Gd}_2[\text{B}]_2\text{O}_7$, where [B] is the B-site cation, is expected to be rather simple compared to other rare-earth pyrochlores since the spin-only ($^8S_{7/2}$) Gd^{3+} ground-state ion should, in principle, display no magnetic anisotropy and therefore exemplify a pure Heisenberg antiferromagnet (HAF) on a pyrochlore lattice. The series crystallizes in the face-centred-cubic $Fd\bar{3}m$ space-group with a range of lattice constants between $10 \lesssim a < 11$ Å. The magnetic rare-earth site lattice is a network of corner-sharing tetrahedral units as depicted in Fig. 1. In the absence of other mechanisms of magnetic exchange, the HAF pyrochlore lattice is predicted to be “fully frustrated” hosting a spin-liquid ground state at low temperatures [6]. In reality, however, near-neighbor antiferromagnetic exchange couplings, J_1 , are generally weak in these systems (well below 1 K), and dipolar field couplings, D_d , are of

comparable strength for near neighbors—see, for example, Refs. [7,8]. For ratios $D_d^1/J_1 \lesssim 5$ (where D_d^1 is the dipolar interaction strength at the first near neighbor), a four-sublattice coplanar $\mathbf{k} = (000)$ antiferromagnetic state, known as the Palmer-Chalker (PC) state [9] (see the depiction in Fig. 1), is predicted with more complex incommensurate orders predicted to appear for $D_d^1/J_1 \gtrsim 5$. In Gd-pyrochlore systems, it is found experimentally using electron spin resonance (ESR) that strong intrashell spin-orbit coupling mixes the $^8S_{7/2}$ and $^6P_{7/2}$ Gd^{3+} levels leading to significant crystal-field splitting and single-ion anisotropy [10]. Table I shows a summary of the properties of Gd-pyrochlore compounds with a variety of B-site cations in order of increasing lattice constant. Common to these materials are their low, negative Weiss temperatures, θ , which slowly decrease in magnitude on increasing lattice constant, and transitions to magnetically long-range-ordered states at temperatures close to 1 K (with the exception of $\text{Gd}_2\text{Ir}_2\text{O}_7$, which has a magnetic B-site cation and does not follow a Curie-Weiss temperature dependence).

The PC state was first looked for by Champion and co-workers [21] in $\text{Gd}_2\text{Ti}_2\text{O}_7$, which displays two magnetic transitions at $T_1 = 1.1$ K and $T_2 = 0.75$ [7,12]. They found, instead, that $\text{Gd}_2\text{Ti}_2\text{O}_7$ exhibits a complex and fascinating *partially ordered* ground state below T_1 . Only recently has the nature of this ground state been revealed to be a complex $2\mathbf{k}$ antiferromagnetic structure with $\mathbf{k} = \{\frac{1}{2} \frac{1}{2} \frac{1}{2}\}$ [20] stabilized by a small ferromagnetic second near-neighbor interaction,

*ross.stewart@stfc.ac.uk

TABLE I. Properties of Gd-pyrochlore compounds with various B-site cations. a is the lattice constant, T_N is the Néel temperature, θ is the Weiss constant, J_1 is the near-neighbor exchange energy, D_d^1 is the dipolar exchange energy at the first near neighbor, D_{SI} is the easy plane single-ion anisotropy, and Δ_{gap} is the spin-wave gap. Values deduced from the current work are asterisked.

B-site	a (Å)	T_N (K)	θ (K)	J_1 (K)	D_d^1 (K)	D_{SI} (K)	Δ_{gap} (meV)
Ge ^a	9.998	1.4	-11.1		0.056		
Ti ^b	10.18	1,0.75 ^d	-9.6	-0.303	0.053	0.223 ^l	0.06 ^m
Pt ^a	10.26	1.6 ^h	-8.8, ^a -9.4 ^h	-0.312*	0.052	0.286*	0.245, ^h 0.25*
Ir ^c	10.29	120,0.65	n/a	-0.23	0.052	0.09	0.21
Sn ^d	10.45	1	-8.6	-0.319 ^j	0.049	0.14 ^l	0.12, ^g 0.13 ⁱ
Hf ^e	10.49	0.77	-7.7	-0.212 ^k	0.049		
Zr ^e	10.52	0.77	-7.3	-0.241 ^k	0.048		
Pb ^f	10.73	0.81	-7.4		0.046		

^aReference [11].

^bReference [7].

^cReference [5].

^dReference [12].

^eReference [13].

^fReference [14].

^gReference [15].

^hReference [16].

ⁱReference [17].

^jReference [18].

^kReference [19].

^lReference [10].

^mReference [20].

shown as J_2 in Fig. 1. Later, neutron diffraction studies by Wills *et al.* of $\text{Gd}_2\text{Sn}_2\text{O}_7$ did find a PC magnetic ground state below $T_N = 1$ K. Additional diffuse and inelastic neutron scattering investigations showed that the PC ground state in

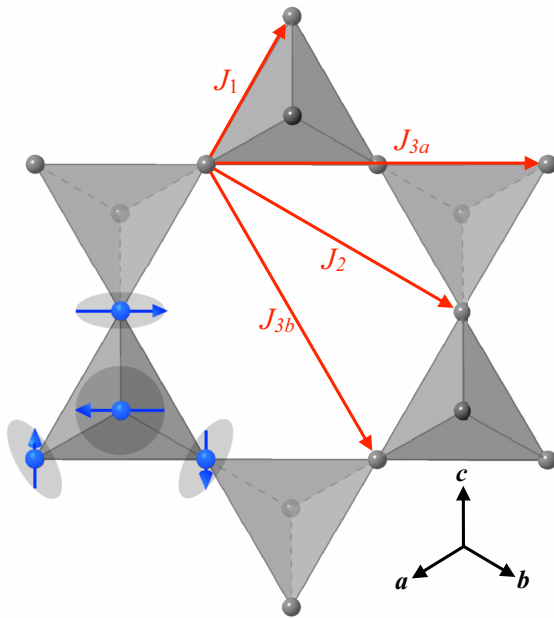


FIG. 1. The A-site rare-earth sublattice in pyrochlore magnets. Principal exchange interaction pathways are shown in red, demonstrating the difference between the two third-nearest-neighbor interactions: the “through-Gd” J_{3a} , which lies parallel to J_1 , and the “cross-hexagon” J_{3b} . The coplanar Palmer-Chalker (PC) spin structure is depicted with blue arrows, bottom left.

$\text{Gd}_2\text{Sn}_2\text{O}_7$ is stabilized by a small ferromagnetic third near-neighbor interaction [18], shown as J_{3b} in Fig. 1. The PC state is also found for the XY-exchange Er-pyrochlore antiferromagnets, $\text{Er}_2\text{Pt}_2\text{O}_7$ and $\text{Er}_2\text{Sn}_2\text{O}_7$ [22,23]. In $\text{Gd}_2\text{Ir}_2\text{O}_7$, the presence of a strongly interacting magnetic B-site sublattice results in a staggered molecular field around the Gd sublattice, which leads to “all-in-all-out” (AIAO) type order at 120 K—a much higher temperature than is commonly found in the series [5]. However, in this system too, the PC state tends to order below 1 K [5]. For all the other Gd-pyrochlore species listed in Table I, the magnetic ground-state structure remains unresolved. This is chiefly due to the enormous difficulty of performing thermal neutron diffraction measurements on Gd containing materials. Naturally occurring Gd metal is the most absorbing element known for thermal neutrons (absorption cross-section $\sigma_{\text{abs}} = 49\,700$ barns for neutron wavelength, $\lambda = 1.8$ Å), meaning that neutron scattering experiments must either be performed using the nonabsorbing (but expensive) ^{160}Gd isotope [17,24,25] or using “hot” neutrons with $\lambda < 0.55$ Å [5,20].

In this study, we present neutron diffraction and inelastic neutron scattering experiments to determine the ground-state magnetic structure and the magnetic interactions in $\text{Gd}_2\text{Pt}_2\text{O}_7$, recently studied by Li *et al.* [11] and Hallas *et al.* [16]. Our sample is enriched with the low neutron-absorbing ^{160}Gd isotope, allowing us to use cold neutrons with wavelengths ≥ 4.8 Å (energies ≤ 3.55 meV)—well suited to the low momentum and energy transfer regimes necessary for studying mK temperature magnetic structures. According to magnetization and specific heat measurements, $\text{Gd}_2\text{Pt}_2\text{O}_7$ orders at 1.6 K, the highest transition temperature in the series (except for $\text{Gd}_2\text{Ir}_2\text{O}_7$). It is suggested by both Li [11] and Hallas [16]

that the presence of empty $5d e_g$ orbitals in Pt^{4+} provides an additional Gd-O-Pt-O-Gd superexchange pathway, leading to the increased magnetic transition temperature. The magnetic susceptibility in $\text{Gd}_2\text{Pt}_2\text{O}_7$ follows closely a Curie-Weiss temperature dependence with a reported Weiss temperature, θ , of $-8.8(1)$ K [11] [$-9.4(1)$ K [16]], which is broadly similar to other Gd-pyrochlores, indicating dominantly antiferromagnetic interactions (see Table I). The Gd magnetic moment is found to be $7.94(1)\mu_B$ [11] [$7.83(1)\mu_B$ [16]], close to the ideal value of $7.94\mu_B$ for spin-only $S = 7/2 \text{ Gd}^{3+}$. The temperature dependence of the specific heat capacity of $\text{Gd}_2\text{Pt}_2\text{O}_7$ closely resembles that of $\text{Gd}_2\text{Sn}_2\text{O}_7$, with a large first-order anomaly at the magnetic ordering temperature. Below T_N , the magnetic specific heat of $\text{Gd}_2\text{Pt}_2\text{O}_7$ has been modeled both using a $C_m \propto T^3$ dependence—expected for a conventional 3D antiferromagnet with an ungapped spin-wave spectrum [11] and with a $C_m \propto \exp(-\Delta_{\text{gap}}/k_B T)/T^2$ dependence expected for a collinear antiferromagnet with a spin-wave gap of $\Delta_{\text{gap}} = 0.245(1)$ meV. [16]. In that work, Hallas and co-workers noted that the presence of a spin-gap in $\text{Gd}_2\text{Sn}_2\text{O}_7$ —confirmed using inelastic neutron scattering [17]—and the similarity of the magnetic specific heat capacities of $\text{Gd}_2\text{Pt}_2\text{O}_7$ and $\text{Gd}_2\text{Sn}_2\text{O}_7$ strongly suggest that the ordered magnetic structure in these materials is the same: the PC state.

We present polarized neutron scattering experiments in both the ordered ($T = 50$ mK) and correlated paramagnetic ($T \geq 1.8$ K) regimes of $\text{Gd}_2\text{Pt}_2\text{O}_7$, and inelastic neutron scattering (INS) measurements of the spin-wave spectrum at 250 mK. We find that the low-temperature magnetic structure of $\text{Gd}_2\text{Pt}_2\text{O}_7$ is indeed the PC state. INS indicates the presence of a gapped spin-wave spectrum at low temperatures, in accordance with the interpretation of Hallas and co-workers [16]. We find from our analysis of INS spectra in the ordered state and diffuse scattering measurements above T_N that the first near-neighbor exchange is of similar strength to other members of the series (see Table I), but that there is also a further near-neighbor Heisenberg exchange (either an antiferromagnetic J_2 or a ferromagnetic J_{3b} interaction) that stabilizes the PC state.

II. EXPERIMENTAL METHODS

The polycrystalline sample used in our neutron scattering experiments was synthesized using high-pressure, high-temperature (HPHT) techniques. A stoichiometric amount of starting material was intimately ground and filled into a gold capsule, and subsequently treated at 1100°C and 6 GPa in a DIA-type cubic diamond anvil high-pressure apparatus,



HPHT synthesis was employed in order to prevent the decomposition of PtO_2 at the temperatures required. The mass of the sample used in each neutron experiment described below was 0.21 g. The nominal enrichment level of the Gd_2O_3 starting material was 99.6% ^{160}Gd .

To determine phase purity, x-ray and neutron diffraction data were collected at room temperature at the I11 high-resolution x-ray diffractometer [26], Diamond Light Source, UK, and the Polaris neutron diffractometer [27], ISIS Neutron

and Muon Source, UK. To minimize absorption during our x-ray diffraction measurements, a portion of our sample was loaded into a 0.1 mm capillary, and data were collected using a multianalyzer crystal (MAC) detector and a wavelength of $\lambda = 0.82658 \text{ \AA}$. Simultaneous Rietveld refinement of these data was carried out using the TOPAS-Academic software package [28].

Investigation of the magnetic exchange interactions in $\text{Gd}_2\text{Pt}_2\text{O}_7$ was undertaken with measurements of the spin-wave excitations in the ordered state using the cold neutron spectrometer LET, at the ISIS Neutron and Muon Source, at an incident energy of 1.60 meV. The sample was mounted in an Oxford Instruments Heliox ^3He sorption insert in a standard helium-flow cryostat and held at 250 mK for the duration of the experiment. Data reduction and normalization to a vanadium standard was performed using MANTID [29]. Linear spin-wave modeling and fitting of the data was performed using SPINW [30].

Neutron diffraction data with XYZ neutron polarization analysis [31] were collected over a range of temperatures between 50 mK and 200 K using a dilution insert in a standard helium-flow cryostat. These measurements were performed on the D7 diffuse scattering spectrometer at the Institut Laue-Langevin (ILL), using an incident neutron wavelength of 4.86 \AA [32,33]. The method of XYZ polarization analysis enables the unambiguous separation of magnetic scattering from nuclear coherent (structural) scattering and nuclear-spin incoherent scattering contributions. The data were corrected for the measured sample self-attenuation, detector, and polarization efficiency using standard samples (vanadium and amorphous silica, respectively), and they were placed on an absolute scale ($\text{barns sr}^{-1} \text{ Gd}^{-1}$), by normalizing the paramagnetic scattering to the paramagnetic moment expected for Gd^{3+} [$g\sqrt{S(S+1)} = 7.94\mu_B$]. For the ordered magnetic and nuclear structures, FULLPROF [34] was used to perform Rietveld refinements, with an interpolated background, and instrumental peak shape parameters from Ref. [33]. The scale factor derived from the nuclear Bragg intensities was employed as an internal check of the absolute normalization of the data. We use mean-field Onsager reaction field (MFO) theory [35,36] in order to estimate exchange interactions in the paramagnetic state. Real-space atomistic models of the paramagnetic scattering are produced via direct Monte Carlo simulations [18] using the SCATTY program [37] to calculate the expected single-crystal diffuse scattering.

III. RESULTS

A. Powder diffraction

Figure 2 shows the neutron and x-ray powder diffraction patterns for $\text{Gd}_2\text{Pt}_2\text{O}_7$ at room temperature, together with a simultaneous Rietveld refinement. Due to the substantial degree of absorption present in these data, a sequential approach to the Rietveld refinements was adopted, exploiting the different sensitivities of x-rays and neutrons in order to avoid the overcorrelation of parameters when absorption coefficients were refined. We refined and fixed the lattice constant using only the x-ray data, followed by using the neutron data to fix the position and the isotropic thermal displacement

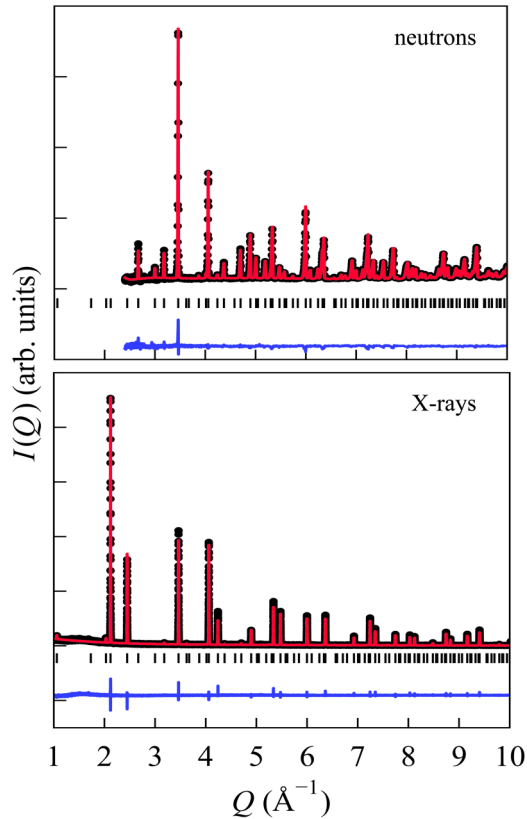


FIG. 2. Neutron (POLARIS bank 5—upper panel) and x-ray (I11—lower panel) diffraction data collected on powder samples of $\text{Gd}_2\text{Pt}_2\text{O}_7$ at room temperature. Red solid lines show the Rietveld refinement of the data, with the difference between the data and model shown in blue.

parameters, $B_{\text{iso}} = 8\pi^2\langle u^2 \rangle$, where $\langle u^2 \rangle$ is the mean-squared displacement of the oxygen atoms. The x-ray data were then used to determine B_{iso} for platinum and gadolinium. The occupancy factors for all the atomic positions were refined using both datasets simultaneously. All the neutron refinements assumed a 100% ^{160}Gd concentration, which introduces a small systematic error in the occupancy refinements. However, the x-ray data are much more sensitive to the Gd-Pt scattering amplitude contrast, and hence the refined occupancies are not significantly affected by this. The refined Bragg R -factors are 4.87% for the I11 x-ray histogram and between 1% and 3.8% for the five diffraction bank histograms on Polaris. Refined structural parameters are given in Table II. All peaks can be indexed using the $Fd\bar{3}m$ cubic space-group; with lattice constant $a = 10.26328(1)\text{Å}$ at 298 K in close agreement with previous results [11,16,38]. The single free O1 coordinate was found to be $x = 0.336$, similar to the value of $x = 0.335$ for $\text{Gd}_2\text{Sn}_2\text{O}_7$ [39]—both larger than the value of $x = 0.326$ found for $\text{Gd}_2\text{Ti}_2\text{O}_7$ [40]. There was no appreciable site mixing of the atomic species with the occupancy factors refining to 1 within experimental uncertainty, indicating full occupancy.

The magnetic neutron diffraction pattern measured at 50 mK using XYZ neutron polarization analysis is shown in Fig. 3 along with the Rietveld refinement of the data. The magnetic scattering is shown fully separated from nuclear and

TABLE II. Atomic positions and occupancies from a simultaneous Rietveld refinement of the x-ray and neutron diffraction data for $\text{Gd}_2\text{Pt}_2\text{O}_7$. In this setting (origin choice 2) of the $Fd\bar{3}m$ space group, the only adjustable atomic coordinate is the x position of O1. * indicates that the value was extracted from x-ray diffraction data, † from neutron diffraction, and ‡ from combined x-ray and neutron diffraction.

Atom	x	y	z	B_{iso}	Occ.
Gd	0.5	0.5	0.5	0.228(5)*	1.000(7)‡
Pt	0	0	0	0.027(3)*	1.000(7)‡
O1	0.33646(6)†	0.125	0.125	0.273(5)†	1.005(6)†
O2	0.375	0.375	0.375	0.296(17)†	0.994(2)‡

incoherent scattering contributions. We observe four magnetic Bragg peaks at 50 mK indicating a transition to a long-range ordered magnetic state. The data are well modeled with the Γ_7 irreducible representation (ψ_6 basis function) following the Kovalev notation [41] used in the paper of Wills and co-workers [25] in describing the PC state in $\text{Gd}_2\text{Sn}_2\text{O}_7$, with a refined Bragg R -factor of 5.25%. This represents the coplanar Palmer-Chalker state. The lattice constant of $\text{Gd}_2\text{Pt}_2\text{O}_7$ at 50 mK is found to be $a = 10.225(1)\text{Å}$ and the ordered Gd magnetic moment is $6.76(2)\mu_B$, which is close to the expected ordered moment value of $gS = 7\mu_B$.

B. Inelastic neutron scattering

Our analysis of the exchange interactions and corresponding Hamiltonian for $\text{Gd}_2\text{Pt}_2\text{O}_7$ begins with our inelastic neutron scattering data taken on LET at 250 mK. Visual inspection of the data, shown for $E_i = 1.60\text{ meV}$ in Fig. 4 (upper panel), reveals several excitation branches—including an approximately flat band at an energy transfer $\Delta E = 0.25\text{ meV}$, gapped from the elastic line. This closely corresponds to the

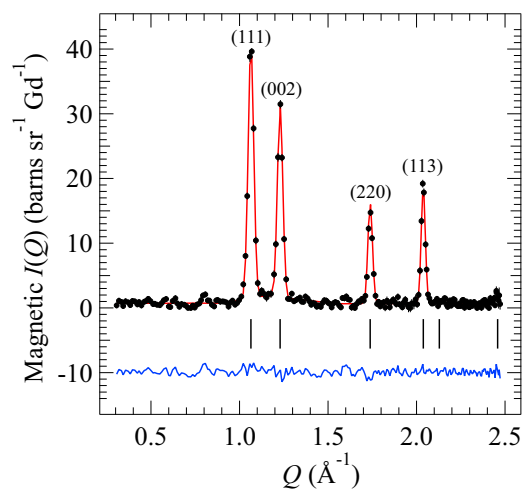


FIG. 3. Magnetic neutron diffraction data measured using XYZ neutron polarization analysis on D7. The red solid line shows the Rietveld refinement using the Γ_7 irreducible representation (ψ_6 basis function) which represents the coplanar Palmer-Chalker antiferromagnet. The difference between the refined model and the data is shown as an offset blue line.

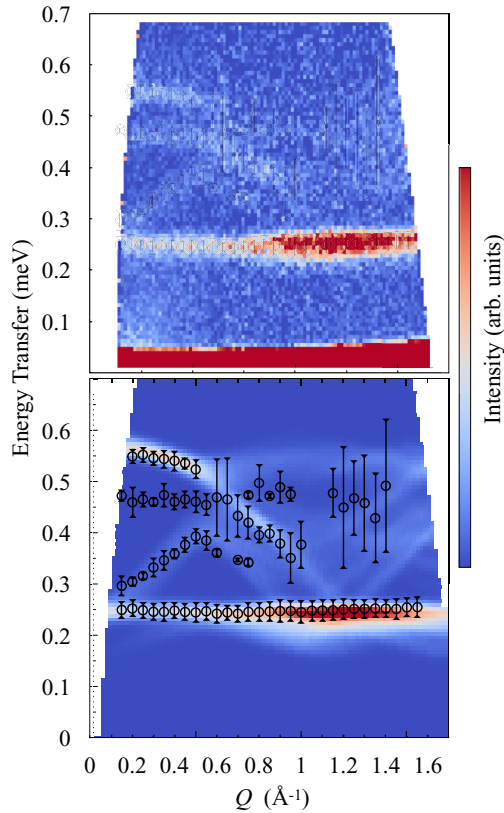


FIG. 4. Upper panel: Inelastic neutron spectra of $\text{Gd}_2\text{Pt}_2\text{O}_7$ at 250 mK taken on LET with incident energy $E_i = 1.6$ meV. The intense region of scattering at zero energy transfer is the nuclear incoherent elastic signal. Lower panel: SPINW calculation of the J_1 - J_2 model $S(\mathbf{Q}, \omega)$ with the best-fit exchange and anisotropy values (see the text). The hollow circles show the positions of the spin-wave peaks found in our data, with the vertical bars representing the FWHM of the peaks. The flat mode at $\Delta E \simeq 0.47$ meV is not reproduced by any of our spin-wave models.

value of the spin-wave gap found by Hallas *et al.* from their modeling of the magnetic heat capacity [16], and it confirms that the excitations are gapped. The observed excitation branches are all absent from spectra taken at high temperatures (>20 K) demonstrating their magnetic origin.

To model the spin-wave excitations, we employ a Hamiltonian containing Heisenberg exchange, dipolar, and single-ion anisotropy terms,

$$H = - \sum_{i>j} J_{ij} \mathbf{S}_i \cdot \mathbf{S}_j + D_{\text{SI}} \sum_i (S_i^z)^2 + D_d^1 r_1^3 \sum_{i>j} \frac{\mathbf{S}_i \cdot \mathbf{S}_j - 3(\mathbf{S}_i \cdot \hat{\mathbf{r}}_{ij})(\mathbf{S}_j \cdot \hat{\mathbf{r}}_{ij})}{r_{ij}^3}, \quad (1)$$

where we have used the convention that negative J -values denote antiferromagnetic interactions. We fix the magnitude of the dipolar energy scale with $D_d^1 = \mu_0(g\mu_B)^2/4\pi r_1^3 k_B = 0.05275$ K, with $\mathbf{r}_1 = (a/4, a/4, 0)$ and $a = 10.225$ Å. The single-ion anisotropy is of the easy-plane type for positive D_{SI} , with the \mathbf{z} -component of the spin-vector S^z lying along local $\langle 111 \rangle$ axes connecting corners of the Gd tetrahedra to the centers [19,42]. We restrict the Heisenberg interactions to

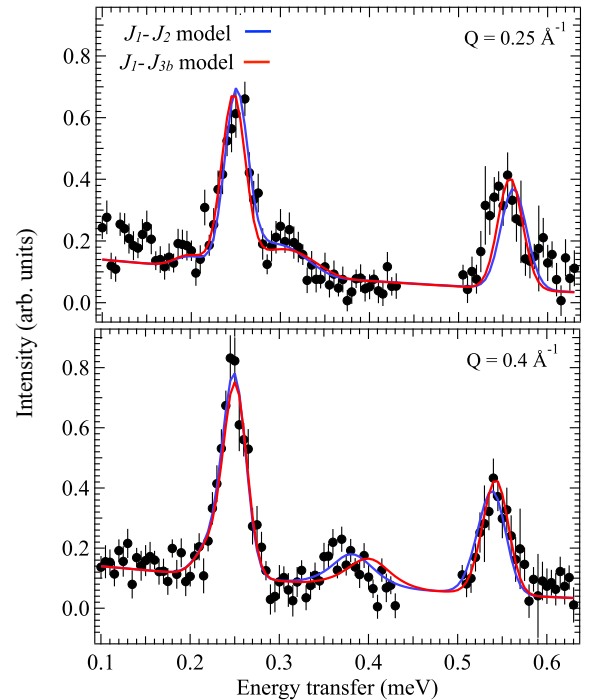


FIG. 5. Constant wave-vector cuts through the spin-wave spectrum of $\text{Gd}_2\text{Pt}_2\text{O}_7$ at $Q = 0.25$ Å $^{-1}$ (upper panel) and $Q = 0.4$ Å $^{-1}$ (lower panel) at $T = 250$ mK. The region between energy transfers of $0.43 < \Delta E \leq 0.5$ meV has been excluded from the fit. The solid lines show the calculated spin-wave scattering using the J_1 - J_2 model (blue) and the J_1 - J_{3b} model (red) plus a linear background.

the first three near-neighbor terms J_1 , J_2 , and J_{3b} as depicted in Fig. 1. We find that the inclusion of J_{3a} (parallel to J_1) does not improve the spin-wave model fits in our analysis.

The spin-wave model is generated from this Hamiltonian using SPINW with the PC state (ψ_6) ordered structure, shown in Fig. 1. In our model, dipolar terms are included up to a range of 20 Å. To calculate the powder-averaged spectrum, the spin-wave cross-sections are calculated for 200 randomly chosen directions of \mathbf{Q} and then averaged. The model calculation is then convoluted with the LET energy and wave-vector resolutions which are taken to be Gaussians of FWHM 30 μeV [calculated for $\Delta E = 0$ meV using PYCHOP (MANTID)] and 0.01 Å $^{-1}$, respectively, at $E_i = 1.6$ meV. This model describes the data well, with the exception of a flat mode observed at $\Delta E \simeq 0.47$ meV, which we are unable to reproduce [see Fig. 4 (lower panel)]. To best fit the exchange interactions and the single-ion anisotropy term, we have performed a least-squares fit of the SPINW generated scattering cross-section to two representative constant wave-vector cuts of the inelastic spectrum at $0.2 < Q \leq 0.3$ and $0.35 < Q \leq 0.45$ Å $^{-1}$. These cuts are shown in Fig. 5 with the best-fit SPINW models. In both of these cuts, we have excluded the energy region around the mode at $\Delta E \simeq 0.47$ meV.

We find that we are able to fit the spin-wave data using spin-wave models employing two different further near-neighbor exchange constants: a $J_1 - J_2$ model and a $J_1 - J_{3b}$ model, shown, respectively, as blue and red solid lines in Fig. 5. The single-ion anisotropy was found to be close to

TABLE III. Fitted exchange interactions and reduced goodness-of-fit (χ^2/N_d) values for each of the fitted spin-wave (SW) and MFO models as described in the main text.

	SW $J_1 - J_2$	SW $J_1 - J_{3b}$	MFO $J_1 - J_2$	MFO $J_1 - J_{3b}$
J_1 (K)	-0.312(2)	-0.312(2)	-0.315(3)	-0.321(2)
J_2 (K)	-0.0073(2)		-0.003(1)	
J_{3b} (K)		0.0070(3)		0.002(1)
χ^2/N_d	1.39	1.49	1.81	1.84

a value of $D_{SI} = 0.286$ K in each of the spin-wave models, and was fixed at this value. The fitted exchange interactions and goodness-of-fit (χ^2/N_d , where N_d is the number of data points) are given in Table III. The spin-wave model covering the entire measured (Q , ΔE) range, calculated using the best-fit exchanges from the $J_1 - J_2$ model, is shown in Fig. 4 (lower panel) with the observed spin-wave peak positions and widths (FWHM) plotted on top. For both the $J_1 - J_2$ and $J_1 - J_{3b}$ spin-wave models, we find $J_1 = -0.312(2)$ K, with an antiferromagnetic second near-neighbor exchange $J_2 \simeq 0.02J_1$ in the $J_1 - J_2$ model, or a *ferromagnetic* cross-hexagon third near-neighbor interaction $J_{3b} \simeq -0.02J_1$ in the $J_1 - J_{3b}$ model. Inspection of each model fit in Fig. 5 shows that the $J_1 - J_2$ spin-wave model better matches the position of the dispersing excitation at $\Delta E \sim 0.73$ meV at $Q = 0.4 \text{ \AA}^{-1}$ and exhibits a marginally lower goodness-of-fit value, as given in Table III.

We also attempted to fit a model with J_1 , J_2 , and J_{3b} all included as free parameters. This did not improve on the $J_1 - J_2$ model fit—and indeed, J_{3b} refined to close to zero within error.

The two spin-wave models describe the data well, apart from the obvious lack of a flat mode at $\Delta E \simeq 0.47$ meV. To try to reproduce this mode, we attempted various more complex models, including anisotropic exchange (unlikely for spin-only Gd ions [43]) and a J_{3a} Heisenberg interaction. Neither of these additions resulted in any measurable improvement to the fit (reduction in χ^2). We investigated the possibility that this mode was spurious—perhaps due to multiple scattering between the sample and the sample environment (e.g., cryostat). However, we found that the mode was present in all the spectra taken at different incident energies, ruling this out. Furthermore, this mode is not present in the spectra taken at higher temperatures, making it certain that it is a real magnetic excitation, and not due to background or structural (phonon) contributions. Of particular interest is the fact that the SPINW model does include a spin-wave branch at this energy, albeit with zero intensity, when the single-crystal dispersions along high-symmetry directions of reciprocal space are calculated. It is possible that symmetry breaking structural features—e.g., oxygen vacancies, site-mixing of gadolinium and platinum—could be responsible for the observed intensity. However, our structural analyses via neutron and x-ray powder diffraction show no evidence of such structural features, as shown in Table II and Fig. 2. Magnetic interactions beyond linear spin-wave theory—e.g., two-magnon processes—have recently been observed in $\text{Yb}_2\text{Ti}_2\text{O}_7$ [44,45], and given the proximity of the mode at 0.47 meV to twice the lower flat band energy of 0.25 meV, it is possible that

two-magnon scattering might play a role here. However, looking carefully at the data in Fig. 4, we note that the expected two-magnon band would be centered at 0.5 meV, directly in between the two high-energy modes at 0.47 and 0.55 meV.

Finally, it is possible that the extra flat mode is due to an excited-state crystal-field transition associated with the single ion anisotropy and admixed higher orbital ground states. In the absence of a crystal field, the ordered moment molecular field splits the $S = \frac{7}{2}$ ground-state multiplet into a ladder of equally spaced levels with spacing $2\mu_B H_{mf}$, with the ground state being a pure $|S_z = \frac{7}{2}\rangle$, the first excited state being $|S_z = \frac{5}{2}\rangle$, and so on. Thus the only dipolar allowed transitions are between adjacent states, where the spin-wave modes are due to the transition between the ground and first excited states. The crystal field, however, will modify this scheme in two ways: first, the admixture of higher multiplets means the wave functions of the $S = \frac{7}{2}$ states will no longer be pure S_z and thus there may be dipole allowed transitions between nonadjacent states; second, the spacing between the states will no longer be a uniform $2\mu_B H_{mf}$. Since the observed 0.47 meV flat mode lies lower in energy than the band maximum, we believe that it is an excited state transition between the thermally occupied first excited state and the second excited state rather than a transition between the ground and (say) second excited states, as this would have a higher energy. Moreover, in the random-phase approximation (RPA), the dispersion bandwidth is proportional to the thermal occupation (Bose) factor, which would naturally be lower for the first excited state than the ground state producing a flatter mode. Finally, if the energy spacing between the states was uniform, one would expect this excited state transition to lie approximately in the middle of the spin wave bandwidth, but this is not the case, suggesting that the crystal field has shifted the relative energies of the $S = \frac{7}{2}$ levels from where they would have been in a pure molecular field. This scenario is still conjecture, however, as we were unable to fit the data with a full RPA calculation using a simple point charge model of the crystal field just including the nearest-neighbor oxygen ligands.

C. Paramagnetic diffuse scattering

The magnetic exchange scheme deduced using inelastic neutron scattering *in the low-temperature ordered phase* can be readily checked by measurement of the magnetic diffuse scattering *in the paramagnetic regime* above T_N . We do this using mean-field Onsager reaction field (MFO) theory in order to calculate the expected magnetic diffuse scattering intensity, $I(Q)$, for a given magnetic exchange scheme. This method has been shown to work well for Heisenberg magnets—see, for example, Refs. [35,46]—and full details of the method are given in Ref. [36].

The magnetic diffuse scattering measured using XYZ polarization analysis on D7 at $T = 1.8, 4,$ and 200 K is presented in Fig. 6 along with MFO fits using the interaction model given by Eq. (1). These data are plotted on an absolute scale in units of (barns $\text{sr}^{-1} \text{Gd}^{-1}$). At $T = 1.8$ K, just above T_N , the data show a broad peak centered at $Q \approx 1.1 \text{ \AA}^{-1}$ along with a decrease in intensity as $Q \rightarrow 0$, indicating strong antiferromagnetic correlations persisting over short distances (lower panel, Fig. 6). The peak decreases in intensity and broadens

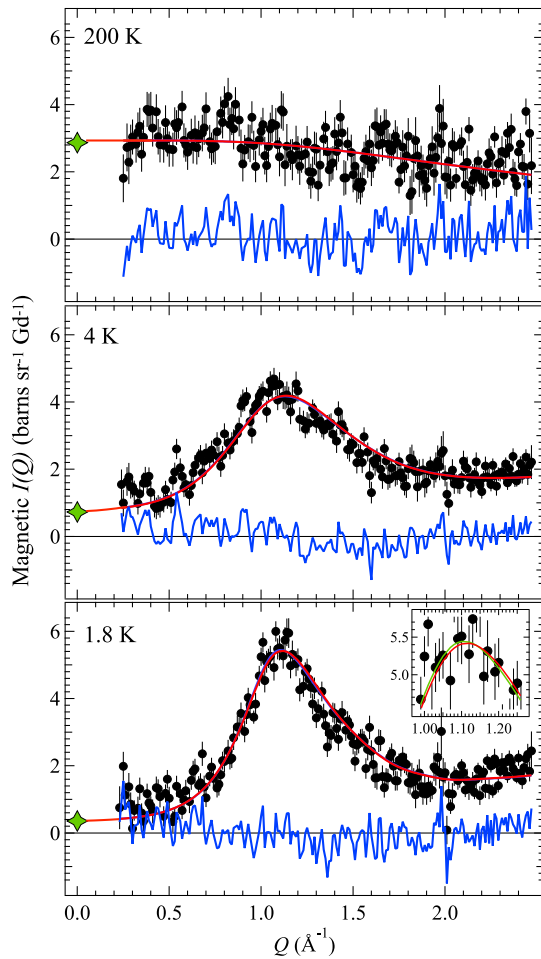


FIG. 6. Paramagnetic diffuse scattering measured using XYZ neutron polarization analysis at 200 K (upper panel), 4 K (middle panel), and 1.8 K (lower panel). The $J_1 - J_2$ MFO model is shown as solid red lines, with the difference between the data and the fit shown as solid blue lines. The inset in the lower panel shows details of the region of peak intensity at $Q \approx 1.1 \text{ \AA}^{-1}$ with both the $J_1 - J_2$ (red) and $J_1 - J_{3b}$ (green) MFO model fits. The stars at $Q = 0$ are the values of the bulk magnetic susceptibility converted to barns $\text{sr}^{-1} \text{Gd}^{-1}$ (see the Appendix).

at 4 K ($2.5T_N$), while at 200 K ($125T_N$) the data follow a squared Gd^{3+} magnetic form-factor dependence, as expected for a fully random paramagnetic spin structure. The MFO fits shown were found to be insensitive to the strength of the single-ion anisotropy, D_{SI} , and therefore this value was fixed to the value $D_{\text{SI}} = 0.286 \text{ K}$ found from our spin-wave fitting. The MFO fits were performed using all three temperatures simultaneously and were also constrained by the susceptibility data of Hallas and co-workers [16]. The $Q = 0$ magnetic cross-section at each temperature, calculated from the bulk susceptibility using the procedure outlined in the Appendix, is plotted in Fig. 6, and the MFO fit to the magnetic susceptibility is shown in Fig. 7. The Weiss temperature extracted from the MFO $J_1 - J_2$ fit in Fig. 7 was found to be $\theta = -9.62(2) \text{ K}$, very close to the value of -9.4 K found by Hallas *et al.*

Similarly to the spin-wave case, we find that $J_1 - J_2$ and $J_1 - J_{3b}$ MFO models both fit the data well. Only slight

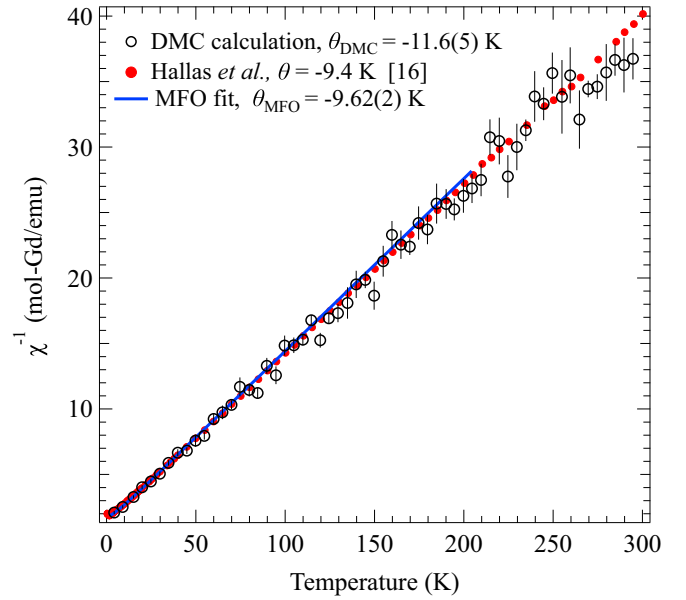


FIG. 7. The inverse magnetic susceptibility of $\text{Gd}_2\text{Pt}_2\text{O}_7$ taken from the paper of Hallas *et al.* [16] (red points). The MFO $J_1 - J_2$ fit to the susceptibility (fitted concurrently with the diffuse magnetic scattering shown in Fig. 6) is shown as a solid blue line. Hollow circles show the inverse susceptibility calculated from our DMC $J_1 - J_2$ model.

differences in the fit are apparent near the peak in intensity at $Q \approx 1.1 \text{ \AA}^{-1}$ at low temperatures [see the inset of Fig. 6 (lower panel)]. As in the spin-wave models, the $J_1 - J_2$ model is a marginally better fit to the data. The best-fit exchange interactions for each model are given in Table III and are found to be in good agreement with the values found via the spin-wave fitting procedure, but with weaker J_2 and J_{3b} values by around a factor of 3. As seen from the high relative uncertainties in J_2 and J_{3b} of $\sim 33\%$, the MFO fits are less sensitive to this interaction than the spin-wave fits, where the relative uncertainties in the further neighbor interactions were found to be $\sim 3\%$. In fact, a reasonable MFO fit was possible with a simple J_1 model and no further near-neighbors—though with a marginally worse goodness of fit, $\chi^2/N_d = 1.86$. Similarly to the spin-wave fits, neither the addition of a third near-neighbor J_{3a} exchange interaction, nor the simultaneous refinement of J_2 and J_{3b} together, improved the quality of the MFO fit.

To compare the spin-correlations predicted by the two models, we use a classical (direct) Metropolis Monte Carlo (DMC) simulation. The simulation was made up of a box of $6 \times 6 \times 6$ unit-cells (containing Gd atoms) with periodic boundaries, interacting via Eq. (1). Long-range dipolar interactions were calculated using Ewald summation. Runs were performed for 5000 moves per spin for equilibration, starting from randomly initialized spin-configurations. The spin auto-correlation function was calculated from snapshots every $t = 500$ moves, and was checked for autocorrelation, with a value of $\langle \mathbf{S}(0) \cdot \mathbf{S}(t) \rangle \lesssim 0.05$ indicating effective decorrelation of the snapshots. Fifty simulation runs were performed for the purposes of averaging. The quality of the models generated using our DMC simulations is checked by comparing the

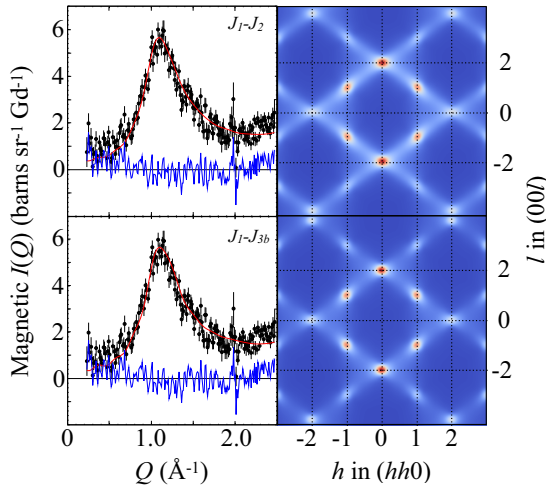


FIG. 8. DMC model of the paramagnetic diffuse scattering in $\text{Gd}_2\text{Pt}_2\text{O}_7$ at 1.8 K. Left column: Calculated magnetic $I(Q)$ (red) shown with the measured magnetic scattering (circles) and the difference curve (blue), for the SW $J_1 - J_2$ model (upper panel) and the SW $J_1 - J_{3b}$ model (lower panel). Right column: Calculated magnetic $I(\mathbf{Q}_{hhl})$ for the $J_1 - J_2$ and $J_1 - J_{3b}$ models.

calculated $I(Q)$ from the DMC model using the Blech-Averbach equation [47] to the data at 1.8 K. We also calculated the magnetic scattering expected from a single-crystal plane of our choosing from our DMC model with the SCATTY software, using the expressions given in Ref. [37]. This is possible from a 3D atomistic magnetic model with the constraints of fixed atomic positions and spin-lengths—and it has been shown to work very successfully in practice [48]. This allows us to directly inspect reciprocal space magnetic correlations alongside real-space spin correlations.

Figure 8 shows the calculated magnetic scattering from the DMC models together with the magnetic scattering data at 1.8 K (same dataset as shown in the lower panel of Fig. 6). These simulations were calculated at $T = 1.8$ K using the fitted exchanges from both the $J_1 - J_2$ and $J_1 - J_{3b}$ spin-wave models. Both models match the measured data well with $\chi^2/N_d = 2.28$ for the $J_1 - J_2$ model and $\chi^2/N_d = 2.47$ for the $J_1 - J_{3b}$ model. Once again, slightly better agreement with the data is found for the $J_1 - J_2$ model. The magnetic $I(\mathbf{Q}_{hhl})$ patterns, calculated for the (hhl) single-crystal plane from these simulations, shown in Fig. 8 are qualitatively identical, showing rods of diffuse scattering along $[111]$ directions. Strong diffuse peaks are evident at the crossing points of these rods of scattering at $\{002\}$ and $\{111\}$ positions (where only one rod is visible in the plane), which are the first two Bragg positions associated with the Palmer-Chalker state, as shown in Fig. 3. Rods of scattering in reciprocal space are associated with planar correlations in real space in the $\{111\}$ planes.

The real-space correlations extracted from the DMC calculations are shown in Fig. 9. The correlations are separated out according to the directions of the exchange interactions, J_1 , J_2 , and J_{3b} — \mathbf{r}_1 , \mathbf{r}_2 , and \mathbf{r}_{3b} , respectively. We find that there are strong spin-correlations along \mathbf{r}_1 , but rather weak correlations along \mathbf{r}_2 and \mathbf{r}_{3b} . This resembles the real-space correlations observed in $\text{Gd}_2\text{Sn}_2\text{O}_7$ and is consistent with planar

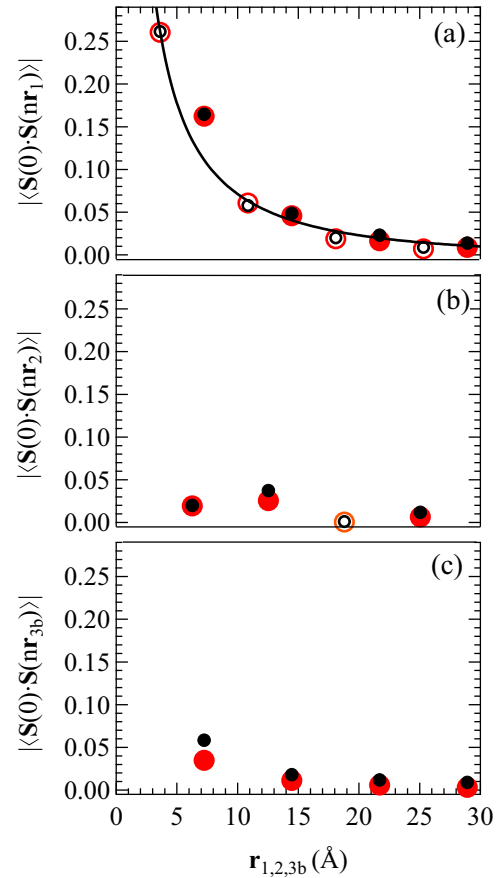


FIG. 9. Real-space correlations in $\text{Gd}_2\text{Pt}_2\text{O}_7$ as a function of distance along each direction parallel to J_1 , J_2 , and J_{3b} — \mathbf{r}_1 , \mathbf{r}_2 , and \mathbf{r}_{3b} shown in (a), (b), and (c), respectively. The hollow symbols denote negative (antiferromagnetic) correlations. The red symbols show correlations taken from the SW $J_1 - J_2$ DMC calculation, while black symbols show those extracted from the SW $J_1 - J_{3b}$ DMC calculation. The solid black line is an Ornstein-Zernike fit to the correlations along \mathbf{r}_1 .

spin-correlations in the $\{111\}$ plane [18]. The spin-correlation length, ξ_1 , at 1.8 K can be roughly estimated via an Ornstein-Zernike form [49], $|\langle \mathbf{S}(0) \cdot \mathbf{S}(\mathbf{r}_1) \rangle| \sim \exp(-r_1/\xi_1)/r_1$, giving $\xi_1 = 53.2(6)$ Å (extracted from the $J_1 - J_2$ model).

The temperature dependence of the magnetic susceptibility can also be calculated from our DMC models using the fluctuation-dissipation formula,

$$\chi T = 1/N \{ \langle M_z^2 \rangle - \langle M_z \rangle^2 \},$$

where M_z is the total magnetization, and the angle brackets denote time averages. This proceeds by running consecutive DMC simulations at temperatures decreasing from 300 K to just above T_N and performing 5000 proposed rotations per spin to achieve equilibrium at each temperature. At least 10^5 proposed moves are then used in calculating the bulk magnetic susceptibility. $\chi(T)$ is converted into units of $\text{emu mol}^{-1}(\text{Gd})$ by multiplying by $N_A \mu_{\text{eff}}^2 k_B^{-1}$ (with $k_B = 1.38 \times 10^{-16}$ erg K^{-1}). Comparison of the calculated $\chi^{-1}(T)$ with the data of Hallas *et al.* [16] is shown in Fig. 7. Calculation of the Weiss temperature from our simulation gives

$\theta = -11.6(5)$ K, close to the value of $\theta = -9.4(1)$ K as determined by Hallas *et al.*

IV. CONCLUSIONS

We have investigated both the ordered magnetic and the correlated paramagnetic regimes of a ^{160}Gd enriched polycrystalline sample of $\text{Gd}_2\text{Pt}_2\text{O}_7$ using neutron diffraction and inelastic neutron scattering. Below T_N we have demonstrated that $\text{Gd}_2\text{Pt}_2\text{O}_7$ orders with the PC state, also found in $\text{Gd}_2\text{Sn}_2\text{O}_7$. We find that two interaction models based on either an antiferromagnetic second near-neighbor interaction (the $J_1 - J_2$ model) or a ferromagnetic cross-hexagon third near-neighbor interaction (the $J_1 - J_{3b}$ model)—both of which are consistent with the $\mathbf{k} = (000)$ PC state—describe well both the inelastic neutron scattering data in the ordered state at low temperatures, and the magnetic diffuse scattering above T_N . In each case, the magnitude of the further neighbor interaction is $\sim 0.02J_1$. The $J_1 - J_2$ model has a slightly better goodness-of-fit value for the spin-wave and MFO fits.

Further near-neighbor interactions are also important in deciding the magnetic ground states of both $\text{Gd}_2\text{Ti}_2\text{O}_7$ and $\text{Gd}_2\text{Sn}_2\text{O}_7$. In $\text{Gd}_2\text{Ti}_2\text{O}_7$, a ferromagnetic second near-neighbor interaction of $J_2 \sim -0.04J_1$ stabilizes its $\mathbf{k} = \{\frac{1}{2} \frac{1}{2} \frac{1}{2}\}$ magnetic structure [20], while in $\text{Gd}_2\text{Sn}_2\text{O}_7$ a ferromagnetic third neighbor interaction of $J_{3b} \sim -0.005J_1$ was found. In $\text{Gd}_2\text{Pt}_2\text{O}_7$ we find that the magnitude of the further neighbor interaction from our spin-wave fits (J_2 or J_{3b}) is $\sim 0.02J_1$ —around four times that of $\text{Gd}_2\text{Sn}_2\text{O}_7$ —which may explain the increased ordering temperature. From our MFO fits we find smaller further neighbor interactions of around $0.007J_1$, very similar to $\text{Gd}_2\text{Sn}_2\text{O}_7$. However, we also find that the MFO fits were much less sensitive to further near-neighbor interactions. As pointed out by Hallas *et al.*, the empty $5d e_g$ orbitals associated with Pt^{4+} are most likely to provide enhanced exchange pathways for both J_2 and J_{3b} —but not for J_1 , where direct Gd-O-Gd pathways are available. This is in agreement with our observation of $J_1 = -0.312$ K, which is very similar to both $\text{Gd}_2\text{Ti}_2\text{O}_7$ and $\text{Gd}_2\text{Sn}_2\text{O}_7$ as can be seen in Table I. The similarity in the magnitudes of J_2 and J_{3b} is likely due to the fact that the superexchange pathway for J_{3b} is identical to that of $J_1 + J_2$. This also explains why the $J_1 - J_2$ and $J_1 - J_{3b}$ models are difficult to distinguish.

ACKNOWLEDGMENTS

The authors would like to gratefully acknowledge the technical and support staff of both the ILL and ISIS, including Xavier Tonon and Chris Lawson, for cryogenic support. We acknowledge ISIS Xpress and Diamond BAG beam time on Polaris and I11, and we are indebted to Ron Smith and Simon Cassidy for conducting these measurements. J.R.S. acknowledges valuable discussions with Lucy Clark and David Vonshen. This work was supported by the UKRI: Engineering and Physical Sciences Research Council and the Science and Facilities Research Council. A portion of this work was supported by the Laboratory Directed Research and Development Program of Oak Ridge National Laboratory, managed by UT-Battelle, LLC for the U.S. Department of Energy.

APPENDIX: $Q = 0$ MAGNETIC SCATTERING AND BULK SUSCEPTIBILITY

The following is the derivation of the $Q = 0$ scattering intensity for magnetic neutron scattering in paramagnets calculated from the bulk susceptibility. We start with the expression for the magnetic cross-section of a paramagnet at $Q = 0$,

$$\left. \frac{d\sigma}{d\Omega} \right|_{Q=0} = \frac{2}{3} \left(\frac{\gamma r_0}{2} \right)^2 g_s^2 S(S+1), \quad (\text{A1})$$

where the factor $(\frac{\gamma r_0}{2})^2 = 0.07265$ barns. The expression for the magnetic susceptibility in SI is given by the Curie law,

$$\chi_{\text{SI}} = \frac{\mu_0 \mu_B^2}{3k_B} g_s^2 S(S+1) \frac{1}{T}. \quad (\text{A2})$$

Combining Eqs. (A2) and (A1), we obtain

$$\left. \frac{d\sigma}{d\Omega} \right|_{Q=0} = 2 \left(\frac{\gamma r_0}{2} \right)^2 \frac{k_B T}{\mu_0 \mu_B^2} \chi_{\text{SI}}. \quad (\text{A3})$$

Note that both the cross-section and the susceptibility are assumed to be normalized per spin. This equation is (within a factor of g_s^2) the same expression as the CGS version given in [50]. It is equivalent to the expression derived via the fluctuation-dissipation theorem and the Kramers-Krönig relation. Generally, the magnetic neutron scattering intensity (differential cross-section) is normalized per magnetic ion (spin), which corresponds to the SI susceptibility given by Eq. (A2) and which has dimensions ($\text{m}^3 \text{spin}^{-1}$).

We must acknowledge the fact that papers generally give susceptibility in CGS units (emu mol^{-1}) or in ($\text{emu mol}_{\text{spins}}^{-1}$), which are related by

$$\chi_{\text{CGS}} (\text{emu mol}_{\text{spins}}^{-1}) = \frac{1}{N_{\text{mag}}} \chi_{\text{CGS}} (\text{emu mol}^{-1}), \quad (\text{A4})$$

where N_{mag} is the number of magnetic ions per formula unit. The CGS expression for the Curie law, with χ_{CGS} in ($\text{emu mol}_{\text{spins}}^{-1}$), is given by

$$\chi_{\text{CGS}} = \frac{N_A \mu_B^2}{3k_B} g_s^2 S(S+1) \frac{1}{T}, \quad (\text{A5})$$

where all the constants are now in CGS; $\mu_B = 9.274 \times 10^{-21}$ erg G $^{-1}$, $k_B = 1.38 \times 10^{-16}$ erg K $^{-1}$, and $N_A = 6.022 \times 10^{23}$ mol $^{-1}$. Gathering these constants together, we can write

$$\frac{N_A \mu_B^2}{3k_B} = \frac{6.022 \times 10^{23} \times 86.0 \times 10^{-42}}{3 \times 1.38 \times 10^{-16}} \simeq \frac{1}{8}, \quad (\text{A6})$$

where this approximation is good to 0.07%. From Eqs. (A2) and (A5), we can now write an expression for converting χ_{SI} to χ_{CGS} ,

$$\chi_{\text{SI}} = \frac{\mu_0 \mu_B^2}{3k_B} \times 8 \chi_{\text{CGS}}. \quad (\text{A7})$$

Finally we can substitute Eq. (A7) into Eq. (A3) to get the expression for the $Q = 0$ cross-section of a paramagnet,

$$\left. \frac{d\sigma}{d\Omega} \right|_{Q=0} = 2 \left(\frac{\gamma r_0}{2} \right)^2 \frac{k_B T}{\mu_0 \mu_B^2} 8 \frac{\mu_0 \mu_B^2}{3k_B} \chi_{\text{CGS}} \quad (\text{A8})$$

$$= \frac{16}{3} \left(\frac{\gamma r_0}{2} \right)^2 T \chi_{\text{CGS}}. \quad (\text{A9})$$

- [1] L. Balents, Spin liquids in frustrated magnets, *Nature (London)* **464**, 199 (2010).
- [2] G. Ehlers, J. E. Greedan, J. R. Stewart, K. C. Rule, P. Fouquet, A. L. Cornelius, C. Adriano, P. G. Pagliuso, Y. Qiu, and J. S. Gardner, High-resolution neutron scattering study of $\text{Tb}_2\text{Mo}_2\text{O}_7$: A geometrically frustrated spin glass, *Phys. Rev. B* **81**, 224405 (2010).
- [3] C. Castelnovo, R. Moessner, and S. L. Sondhi, Magnetic monopoles in spin ice, *Nature (London)* **451**, 42 (2008).
- [4] S. Petit, E. Lhotel, B. Canals, M. Ciomaga Hatnean, J. Ollivier, H. Mutka, E. Ressouche, A. R. Wildes, M. R. Lees, and G. Balakrishnan, Observation of magnetic fragmentation in spin ice, *Nat. Phys.* **12**, 746 (2016).
- [5] E. Lefrançois, L. Mangin-Thro, E. Lhotel, J. Robert, S. Petit, V. Cathelin, H. E. Fischer, C. V. Colin, F. Damay, J. Ollivier, P. Lejay, L. C. Chapon, V. Simonet, and R. Ballou, Spin decoupling under a staggered field in the $\text{Gd}_2\text{Ir}_2\text{O}_7$ pyrochlore, *Phys. Rev. B* **99**, 060401(R) (2019).
- [6] J. N. Reimers, Absence of long-range order in a three-dimensional geometrically frustrated antiferromagnet, *Phys. Rev. B* **45**, 7287 (1992).
- [7] N. P. Raju, M. Dion, M. J. P. Gingras, T. E. Mason, and J. E. Greedan, Transition to long-range magnetic order in the highly frustrated insulating pyrochlore antiferromagnet $\text{Gd}_2\text{Ti}_2\text{O}_7$, *Phys. Rev. B* **59**, 14489 (1999).
- [8] A. P. Ramirez, B. S. Shastry, A. Hayashi, J. J. Krajewski, D. A. Huse, and R. J. Cava, Multiple Field-Induced Phase Transitions in the Geometrically Frustrated Dipolar Magnet: $\text{Gd}_2\text{Ti}_2\text{O}_7$, *Phys. Rev. Lett.* **89**, 067202 (2002).
- [9] S. E. Palmer and J. T. Chalker, Order induced by dipolar interactions in a geometrically frustrated antiferromagnet, *Phys. Rev. B* **62**, 488 (2000).
- [10] V. N. Glazkov, M. E. Zhitomirsky, A. I. Smirnov, H.-A. K. von Nidda, A. Loidl, C. Marin, and J. P. Sanchez, Single-ion anisotropy in the gadolinium pyrochlores studied by electron paramagnetic resonance, *Phys. Rev. B* **72**, 020409(R) (2005).
- [11] X. Li, Y. Q. Cai, Q. Cui, C. J. Lin, Z. L. Dun, K. Matsubayashi, Y. Uwatoko, Y. Sato, T. Kawae, S. J. Lv, C. Q. Jin, J.-S. Zhou, J. B. Goodenough, H. D. Zhou, and J.-G. Cheng, Long-range magnetic order in the Heisenberg pyrochlore antiferromagnets $\text{Gd}_2\text{Ge}_2\text{O}_7$ and $\text{Gd}_2\text{Pt}_2\text{O}_7$ synthesized under high pressure, *Phys. Rev. B* **94**, 214429 (2016).
- [12] P. Bonville, J. A. Hodges, M. Ocio, J. P. Sanchez, P. Vulliet, S. Sosin, and D. Braithwaite, Low temperature properties of geometrically frustrated $\text{Gd}_2\text{Sn}_2\text{O}_7$ and $\text{Gd}_2\text{Ti}_2\text{O}_7$, *J. Phys.: Condens. Matter* **15**, 7777 (2003).
- [13] A. M. Durand, P. Klavins, and L. R. Corruccini, Heat capacity of the frustrated magnetic pyrochlores $\text{Gd}_2\text{Zr}_2\text{O}_7$ and $\text{Gd}_2\text{Hf}_2\text{O}_7$, *J. Phys.: Condens. Matter* **20**, 235208 (2008).
- [14] A. M. Hallas, A. M. Arevalo-Lopez, A. Z. Sharma, T. Munsie, J. P. Attfield, C. R. Wiebe, and G. M. Luke, Magnetic frustration in lead pyrochlores, *Phys. Rev. B* **91**, 104417 (2015).
- [15] J. A. Quilliam, K. A. Ross, A. G. Del Maestro, M. J. P. Gingras, L. R. Corruccini, and J. B. Kycia, Evidence for Gapped Spin-Wave Excitations in the Frustrated $\text{Gd}_2\text{Sn}_2\text{O}_7$ Pyrochlore Antiferromagnet from Low-Temperature Specific Heat Measurements, *Phys. Rev. Lett.* **99**, 097201 (2007).
- [16] A. M. Hallas, A. Z. Sharma, Y. Cai, T. J. Munsie, M. N. Wilson, M. Tachibana, C. R. Wiebe, and G. M. Luke, Relief of frustration in the Heisenberg pyrochlore antiferromagnet $\text{Gd}_2\text{Pt}_2\text{O}_7$, *Phys. Rev. B* **94**, 134417 (2016).
- [17] J. R. Stewart, J. S. Gardner, Y. Qiu, and G. Ehlers, Collective dynamics in the Heisenberg pyrochlore antiferromagnet $\text{Gd}_2\text{Sn}_2\text{O}_7$, *Phys. Rev. B* **78**, 132410 (2008).
- [18] J. A. M. Paddison, G. Ehlers, O. A. Petrenko, A. R. Wildes, J. S. Gardner, and J. R. Stewart, Spin correlations in the dipolar pyrochlore antiferromagnet $\text{Gd}_2\text{Sn}_2\text{O}_7$, *J. Phys. Condens. Matter* **29**, 144001 (2017).
- [19] A. A. Biswas and Y. M. Jana, Estimation of single-ion anisotropies, crystal-field and exchange interactions in Gd-based frustrated pyrochlore anti-ferromagnets $\text{Gd}_2\text{M}_2\text{O}_7$ ($M = \text{Ti}, \text{Sn}, \text{Hf}, \text{Zr}$), *J. Magn. Magn. Mater.* **323**, 3202 (2011).
- [20] J. A. M. Paddison, G. Ehlers, A. B. Cairns, J. S. Gardner, O. A. Petrenko, N. P. Butch, D. D. Khalyavin, P. Manuel, H. E. Fischer, H.-D. Zhou, A. L. Goodwin, and J. R. Stewart, Suppressed-moment 2-k order in the canonical frustrated antiferromagnet $\text{Gd}_2\text{Ti}_2\text{O}_7$, *npj Quantum Mater.* **6**, 99 (2021).
- [21] J. D. M. Champion, A. S. Wills, T. Fennell, S. T. Bramwell, J. S. Gardner, and M. A. Green, Order in the Heisenberg pyrochlore: The magnetic structure of $\text{Gd}_2\text{Ti}_2\text{O}_7$, *Phys. Rev. B* **64**, 140407(R) (2001).
- [22] A. M. Hallas, J. Gaudet, N. P. Butch, G. Xu, M. Tachibana, C. R. Wiebe, G. M. Luke, and B. D. Gaulin, Phase Competition in the Palmer-Chalker XY Pyrochlore $\text{Er}_2\text{Pt}_2\text{O}_7$, *Phys. Rev. Lett.* **119**, 187201 (2017).
- [23] S. Petit, E. Lhotel, F. Damay, P. Boutrouille, A. Forget, and D. Colson, Long-Range Order in the Dipolar XY Antiferromagnet $\text{Er}_2\text{Sn}_2\text{O}_7$, *Phys. Rev. Lett.* **119**, 187202 (2017).
- [24] J. R. Stewart, G. Ehlers, A. S. Wills, S. T. Bramwell, and J. S. Gardner, Phase transitions, partial disorder and multi-k structures in $\text{Gd}_2\text{Ti}_2\text{O}_7$, *J. Phys.: Condens. Matter* **16**, L321 (2004).
- [25] A. S. Wills, M. E. Zhitomirsky, B. Canals, J. P. Sanchez, P. Bonville, P. D. de Réotier, and A. Yaouanc, Magnetic ordering in $\text{Gd}_2\text{Sn}_2\text{O}_7$: the archetypal Heisenberg pyrochlore antiferromagnet, *J. Phys.: Condens. Matter* **18**, L37 (2006).
- [26] S. P. Thompson, J. E. Parker, J. Potter, T. P. Hill, A. Birt, T. M. Cobb, F. Yuan, and C. C. Tang, Beamline I11 at diamond: A new instrument for high resolution powder diffraction, *Rev. Sci. Instrum.* **80**, 075107 (2009).
- [27] R. I. Smith, S. Hull, M. G. Tucker, H. Y. Playford, D. J. McPhail, S. P. Waller, and S. T. Norberg, The upgraded Polaris powder diffractometer at the ISIS neutron source, *Rev. Sci. Instrum.* **90**, 115101 (2019).
- [28] A. A. Coelho, *TOPAS* and *topas-academic*: An optimization program integrating computer algebra and crystallographic objects written in C++, *J. Appl. Crystallogr.* **51**, 210 (2018).
- [29] O. Arnold, J. C. Bilheux, J. M. Borreguero, A. Buts, S. I. Campbell, L. Chapon, M. Doucet, N. Draper, R. Ferraz Leal, M. A. Gigg, V. E. Lynch, A. Markvardsen, D. J. Mikkelsen, R. L. Mikkelsen, R. Miller, K. Palmén, P. Parker, G. Passos, T. G. Perring, P. F. Peterson *et al.*, Mantid—Data analysis and visualization package for neutron scattering and μ SR experiments, *Nucl. Instrum. Methods Phys. Res. A* **764**, 156 (2014).
- [30] S. Toth and B. Lake, Linear spin wave theory for single-Q incommensurate magnetic structures, *J. Phys.: Condens. Matter* **27**, 166002 (2015).
- [31] O. Schärpf and H. Capellmann, The xyz-difference method with polarized neutrons and the separation of coherent, spin

- incoherent, and magnetic scattering cross sections in a multi-detector, *Phys. Status Solidi C* **135**, 359 (1993).
- [32] J. R. Stewart, P. P. Deen, K. H. Andersen, H. Schober, J.-F. Barthélemy, J. M. Hillier, A. P. Murani, T. Hayes, and B. Lindenau, Disordered materials studied using neutron polarization analysis on the multi-detector spectrometer, D7, *J. Appl. Crystallogr.* **42**, 69 (2009).
- [33] T. Fennell, L. Mangin-Thro, H. Mutka, G. J. Nilsen, and A. R. Wildes, Wavevector and energy resolution of the polarized diffuse scattering spectrometer D7, *Nucl. Instrum. Methods Phys. Res.* **857**, 24 (2017).
- [34] J. Rodríguez-Carvajal, Recent advances in magnetic structure determination by neutron powder diffraction, *Physica B* **192**, 55 (1993).
- [35] D. Hohlwein, J.-U. Hoffmann, and R. Schneider, Magnetic interaction parameters from paramagnetic diffuse neutron scattering in MnO, *Phys. Rev. B* **68**, 140408(R) (2003).
- [36] J. A. M. Paddison, Scattering Signatures of Bond-Dependent Magnetic Interactions, *Phys. Rev. Lett.* **125**, 247202 (2020).
- [37] J. A. M. Paddison, Ultrafast calculation of diffuse scattering from atomistic models, *Acta Crystallogr. Sect. A* **75**, 14 (2019).
- [38] H. R. Hoekstra and F. Gallagher, Synthesis of some pyrochlore-type oxides of platinum (IV) at high pressure, *Inorg. Chem.* **7**, 2553 (1968).
- [39] B. J. Kennedy, B. A. Hunter, and C. J. Howard, Structural and bonding trends in tin pyrochlore oxides, *J. Solid State Chem.* **130**, 58 (1997).
- [40] K. B. Helean, S. V. Ushakov, C. E. Brown, A. Navrotsky, J. Lian, R. C. Ewing, J. M. Farmer, and L. A. Boatner, Formation enthalpies of rare earth titanate pyrochlores, *J. Solid State Chem.* **177**, 1858 (2004).
- [41] O. V. Kovalev, *Representations of the Crystallographic Space Groups*, 2nd ed. (Gordon and Breach, Switzerland, 1993).
- [42] V. N. Glazkov, A. I. Smirnov, J. P. Sanchez, A. Forget, D. Colson, and P. Bonville, Electron spin resonance study of the single-ion anisotropy in the pyrochlore antiferromagnet $\text{Gd}_2\text{Sn}_2\text{O}_7$, *J. Phys.: Condens. Matter* **18**, 2285 (2006).
- [43] H. Yan, O. Benton, L. Jaubert, and N. Shannon, Theory of multiple-phase competition in pyrochlore magnets with anisotropic exchange with application to $\text{Yb}_2\text{Ti}_2\text{O}_7$, $\text{Er}_2\text{Ti}_2\text{O}_7$, and $\text{Er}_2\text{Sn}_2\text{O}_7$, *Phys. Rev. B* **95**, 094422 (2017).
- [44] J. D. Thompson, P. A. McClarty, D. Prabhakaran, I. Cabrera, T. Guidi, and R. Coldea, Quasiparticle Breakdown and Spin Hamiltonian of the Frustrated Quantum Pyrochlore $\text{Yb}_2\text{Ti}_2\text{O}_7$ in a Magnetic Field, *Phys. Rev. Lett.* **119**, 057203 (2017).
- [45] J. G. Rau, R. Moessner, and P. A. McClarty, Magnon interactions in the frustrated pyrochlore antiferromagnet $\text{Yb}_2\text{Ti}_2\text{O}_7$, *Phys. Rev. B* **100**, 104423 (2019).
- [46] P. H. Conlon and J. T. Chalker, Absent pinch points and emergent clusters: Further neighbor interactions in the pyrochlore Heisenberg antiferromagnet, *Phys. Rev. B* **81**, 224413 (2010).
- [47] I. A. Blech and B. L. Averbach, Spin correlations in MnO, *Physics* **1**, 31 (1964).
- [48] J. A. M. Paddison and A. L. Goodwin, Empirical Magnetic Structure Solution of Frustrated Spin Systems, *Phys. Rev. Lett.* **108**, 017204 (2012).
- [49] W. G. Stirling and S. C. Perry, Critical scattering, *PSI Proceedings 96-01* (Paul Scherrer Institute, 1996), Ch. 5.
- [50] N. Ahmed and T. J. Hicks, Polarization analysis of neutron scattering from CuMn alloys, *Solid State Commun.* **15**, 415 (1974).